

**AEDC-TR-92-12**

**AD-A256 784**



2

**Analysis of the AlCl Absorption Feature and  
the Searchlight Emission Effect Observed  
in Solid-Propellant Rocket Plumes**

S. M. Oliver, W. K. McGregor, R. A. Reed, and J. A. Drakes, et al.  
Sverdrup Technology, Inc., AEDC Group

September 1992

**DTIC**  
**ELECTE**  
**S, D**  
**OCT. 22 1992**

Final Report for Period October 1991 through July 1992

Approved for public release; distribution is unlimited.

92 10 20 102

042550

**92-27561**



4328

**ARNOLD ENGINEERING DEVELOPMENT CENTER  
ARNOLD AIR FORCE BASE, TENNESSEE  
AIR FORCE MATERIEL COMMAND  
UNITED STATES AIR FORCE**

### NOTICES

When U. S. Government drawings, specifications, or other data are used for any purpose other than a definitely related Government procurement operation, the Government thereby incurs no responsibility nor any obligation whatsoever, and the fact that the Government may have formulated, furnished, or in any way supplied the said drawings, specifications, or other data, is not to be regarded by implication or otherwise, or in any manner licensing the holder or any other person or corporation, or conveying any rights or permission to manufacture, use, or sell any patented invention that may in any way be related thereto.

Qualified users may obtain copies of this report from the Defense Technical Information Center.

References to named commercial products in this report are not to be considered in any sense as an endorsement of the product by the United States Air Force or the Government.

This report has been reviewed by the Office of Public Affairs (PA) and is releasable to the National Technical Information Service (NTIS). At NTIS, it will be available to the general public, including foreign nations.

### APPROVAL STATEMENT

This report has been reviewed and approved.

*David G. Burgess*

DAVID G. BURGESS, Capt, USAF  
Directorate of Technology  
Deputy for Operations

Approved for publication:

FOR THE COMMANDER

*Keith L. Kushman*

KEITH L. KUSHMAN  
Director of Technology  
Deputy for Operations

REPORT DOCUMENTATION PAGE			Form Approved OMB No. 0704-0188	
Public reporting burden for this collection of information is estimated to average 1 hour per response, including the time for reviewing instructions, searching existing data sources, gathering and maintaining the data needed, and completing and reviewing the collection of information. Send comments regarding this burden estimate or any other aspect of this collection of information, including suggestions for reducing this burden, to Washington Headquarters Services, Directorate for Information Operations and Reports, 1215 Jefferson Davis Highway, Suite 1204, Arlington, VA 22202-4302, and to the Office of Management and Budget, Paperwork Reduction Project (0704-0188), Washington, DC 20503.				
1. AGENCY USE ONLY (Leave blank)	2. REPORT DATE September 1992	3. REPORT TYPE AND DATES COVERED Final - 1976-91 - 30 Sep 92		
4. TITLE AND SUBTITLE  Analysis of the AlCl Absorption Feature and the Searchlight Emission Effect Observed in Solide-Propellant Rocket Plumes		5. FUNDING NUMBERS		
6. AUTHOR(S) Oliver, S. M., McGregor, W. K., Reed, R. A., Drakes, J. A., Beale, K. S., Sherrell, F. G., and Neese, D. W., Sverdrup Technology, Inc., AEDC Group		ARO MIPR 131-91		
7. PERFORMING ORGANIZATION NAME(S) AND ADDRESS(ES)  Arnold Engineering Development Center/DOF Air Force Materiel Command Arnold Air Force Base, TN 37389-5000		8. PERFORMING ORGANIZATION REPORT NUMBER  AEDC-TR-92-12		
9. SPONSORING/MONITORING AGENCY NAME(S) AND ADDRESS(ES)  Army Research Organization (ARO) P. O. Box 12211 Research Triangle Park, NC 27709-2211		10. SPONSORING/MONITORING AGENCY REPORT NUMBER  ARO 28912.3-EG-SDF		
11. SUPPLEMENTARY NOTES  Available in Defense Technical Information Center (DTIC).				
12a. DISTRIBUTION/AVAILABILITY STATEMENT  Approved for public release; distribution is unlimited.		12b. DISTRIBUTION CODE		
13. ABSTRACT (Maximum 200 words)  Two phenomena observed during plume diagnostic measurements acquired during simulated altitude chamber tests of aluminum-loaded solid-propellant rocket motors are discussed, and analytical results are presented. The results of a line-by-line calculation of the aluminum chloride (AlCl) feature are discussed and compared with high-resolution ultraviolet (UV) spectral data. Selected plume radiation measurements are reviewed, and evidence of searchlight emission is presented. Two searchlight modeling techniques are demonstrated and compared with motor test data.				
14. SUBJECT TERMS AlCl absorption searchlight plume radiation		plumes infrared ultraviolet		15. NUMBER OF PAGES 42
		solid-propellant rocket motor line-by-line calculation Monte Carlo		16. PRICE CODE
17. SECURITY CLASSIFICATION OF REPORT UNCLASSIFIED	18. SECURITY CLASSIFICATION OF THIS PAGE UNCLASSIFIED	19. SECURITY CLASSIFICATION OF ABSTRACT UNCLASSIFIED		20. LIMITATION OF ABSTRACT  SAME AS REPORT

## PREFACE

The work reported herein was conducted at the Arnold Engineering Development Center at the request of the Army Research Organization (ARO). Dr. David Mann was the ARO Project Officer. The results of the tests were obtained by Sverdrup Technology, Inc., AEDC Group (a Sverdrup Corporation Company), support contractor of the propulsion test facilities, AEDC, Air Force Materiel Command (AFMC), Arnold Air Force Base, Tennessee. The AEDC Air Force Program Manager was Capt. D. G. Burgess. The Sverdrup Project Managers were S. M. Oliver and K. S. Beale.

The authors acknowledge helpful discussions with Drs. D. Nelson of the Aerospace Corporation, J. E. Reardon and J. Everson of Remtech, Inc., L. S. Bernstein and M. Zakin of Spectral Sciences, Inc., H. F. Nelson of the University of Missouri at Rolla, M. W. Slack of Lockheed Missiles and Space Corporation, and S. Rudmann of Grumman Aerospace. The nozzle lip temperature calculations were performed by Dr. P. Melia, United Technologies Chemical Systems Division. The laser transmission measurements were performed by D. B. Cox of Sverdrup Technology and P. J. Murphy of OptiLogic, Inc. V. A. Zaccardi was the Sverdrup project manager for several of the motor tests, and M. A. Simmons, also of Sverdrup Technology, provided plume flow-field code predictions.

DTIC QUALITY INSPECTED 1

<b>Accession For</b>	
NTIS GRA&I	<input checked="checked" type="checkbox"/>
DTIC TAB	<input type="checkbox"/>
Unannounced	<input type="checkbox"/>
Justification	
By _____	
Distribution/	
Availability Codes	
Dist	Avail and/or Special
A-1	

## CONTENTS

	<u>Page</u>
1.0 INTRODUCTION .....	7
2.0 ALUMINUM CHLORIDE ABSORPTION ANALYSIS .....	7
2.1 Introduction .....	7
2.2 Spectra Description .....	7
2.3 AlCl Molecule .....	8
2.4 Radiative Transfer Model .....	8
2.5 Modeling Results .....	12
2.6 Conclusions .....	14
3.0 SEARCHLIGHT EMISSION ANALYSIS .....	14
3.1 Introduction .....	14
3.2 Searchlight Mechanism .....	15
3.3 Plume Radiation Measurements .....	18
3.4 Monte Carlo Estimate of Searchlight Intensity .....	20
3.5 Summary .....	23
4.0 SUMMARY .....	24
REFERENCES .....	24

## ILLUSTRATIONS

<u>Figure</u>	<u>Page</u>
1. Schematic of Solid-Propellant Rocket Motor Test Configuration Used for UV Spectral Measurements .....	27
2. Moderate-Resolution Mid-UV Spectra from Solid-Propellant Rocket Motor Plume .....	28
3. High-Resolution UV Spectra from Solid-Propellant Rocket Motor Plume .....	28
4. Predicted Radial Profiles for Solid-Propellant Rocket Motor at Axial Location where UV Spectra were Measured (Standard Plume Flow-Field Code Using Three Particle Groups) .....	29
5. Physical Model of Solid-Propellant Rocket Motor Plume UV Spectral Measurement Experiment .....	30
6. Comparison of Computed with Measured Spectra of SRM Plume Radiation at Predicted Plume Conditions .....	30

<u>Figure</u>	<u>Page</u>
7. Comparison of Computed with Measured Spectra of SRM Plume Radiation at "Best Fit" Conditions .....	31
8. Sketch of Searchlight Emission where Small Angle Scattering by Plume $\text{Al}_2\text{O}_3$ Droplets and Particles Redirects Nozzle Emission toward Broadside Radiometers .....	31
9. Mie Scattering Albedo of 3- $\mu\text{m}$ -Radius $\text{Al}_2\text{O}_3$ Droplet .....	32
10. Scattering Phase Function of $\text{Al}_2\text{O}_3$ Droplet at Three Wavelengths .....	32
11. Geometry of Gedanken Experiment Showing Radiance of a Reflecting and Emitting Sphere Suspended above a Hot Plate .....	33
12. Motor A Thrust and SWIR Radiance Time Histories .....	33
13. Radiative Heat Flux at Three Locations for Motor A .....	34
14. Normalized Thrust, SWIR, and LWIR Time Histories for Motor B .....	34
15. Power Spectral Density Comparison of Thrust Versus Short Wavelength Infrared (SWIR) Radiance .....	35
16. Calculated Radiance of Motor B Nozzle Lip at Two Wavelengths .....	35
17. Decomposition of Motor B Radiance into Searchlight and Plume Emission Based upon Calculated Nozzle Lip Temperature Time History .....	36
18. Extinction Coefficient for Motor A where Inversions at Approximately 1-sec Intervals are Shown near the Beginning and the End of the Burn .....	36
19. Monte Carlo Calculation of Searchlight for Motor A for Radiometers Located at 2-, 17-, and 29-in. Axial Position where the Nozzle Exit Plane is at 0 cm and the Table Gives Searchlight View Factor for Each Radiometer .....	37
20. Monte Carlo Calculation of Searchlight View Factor Versus Viewing Aspect Angle where Radiometer Location is 2 in. Downstream of Nozzle Exit Plane .....	37

## TABLES

	<u>Page</u>
1. Bandheads of the AlCl A <sup>1</sup> Π - X <sup>1</sup> Σ System .....	38
2. Molecular Constants for the Ground and Resonant States of Al <sup>35</sup> Cl (cm <sup>-1</sup> ) .....	39
3. Einstein Coefficients for the A <sup>1</sup> Π - X <sup>1</sup> Σ <sup>+</sup> Transition in AlCl (Ref. 7) .....	39
4. Constants for Dunham Level Expression of Energy Level of the X <sup>1</sup> Σ State of AlCl .....	40

## 1.0 INTRODUCTION

Plume diagnostic measurements conducted at Arnold Engineering Development Center (AEDC) on several solid-propellant rocket exhausts have revealed phenomena which may provide insight into the characterization of these plumes. Two of these phenomena, aluminum chloride (AlCl) absorption and searchlight emission, are highlighted in this report. Modeling of each phenomenon and comparison of predictions with plume measurements acquired during simulated altitude chamber tests are also presented.

A discussion is presented in Section 2.0 on the analysis of the AlCl absorption feature observed in aluminized solid-propellant rocket plumes. The results of a line-by-line calculation are discussed and compared with high-resolution ultraviolet (UV) spectral data.

In Section 3.0, selected plume radiation measurements are reviewed, and evidence of searchlight emission is presented. Two modeling approaches are discussed and compared with motor test data.

## 2.0 ALUMINUM CHLORIDE ABSORPTION ANALYSIS

### 2.1 INTRODUCTION

An interesting feature in the mid-ultraviolet spectrum of the radiation from aluminized solid-propellant rocket exhausts has been noted several times in unpublished reports. This feature is a deep absorption near 262 nm of the otherwise continuum spectrum typical of hot aluminum oxide particles. It has been attributed to the AlCl A-X transition, although the spectral resolution was not sufficient to resolve bandheads (Ref. 1). Recently, spectra were obtained having sufficient resolution to identify the vibrational bands, and these will be reported here. Curiously, spectra obtained from an onboard spectrometer viewing an in-flight rocket plume having an aluminized propellant also contained this feature (Ref. 2).

One obvious question arising from such an inherent spectral feature is whether it can be used to diagnose any properties of the rocket exhaust flow. To that end, a modeling effort was undertaken, and this paper reports on the success of that work.

### 2.2 SPECTRA DESCRIPTION

When a moderate-resolution (0.8 nm) ultraviolet scanning monochromator is pointed normal to the axis of an exhaust plume from an aluminized solid-propellant rocket motor being fired in an altitude test cell (Fig. 1), the spectra shown in Fig. 2 result. The continuum on either side of the feature at 262 nm and the thermal behavior of the radiation in the visible



and infrared regions suggests that the feature is caused by the absorption of a gaseous specie. A quick examination of the predicted products of combustion of ammonium perchlorate with aluminum and hydrocarbon solids, along with a trip through Pearse and Gaydon's (Ref. 3) atlas of spectra, reveals that the most likely absorber is AlCl. To investigate this identification more thoroughly, higher-resolution spectra were obtained during a subsequent test. Because of the small vibrational (approximately  $450\text{ cm}^{-1}$ ) and rotational (approximately  $0.25\text{ cm}^{-1}$ ) constants of both AlCl states, a spectral resolution of about  $0.1\text{ nm}$  was required to produce the band structure. The resulting spectrum (Fig. 3) indeed does show the expected structure, and many of the bands listed in Pearse and Gaydon (Table 1) are identified.

### 2.3 AlCl MOLECULE

Aluminum chloride sublimates at temperatures above  $460\text{ K}$ . A calculation of the plume properties using the JANNAF standard plume flow-field codes (Ref. 4) gives the solid and gaseous temperature profiles of Fig. 4a for this particular rocket plume. The minimum predicted temperature is about  $600\text{ K}$  so that the AlCl is gaseous. Furthermore, the predicted mole fraction of AlCl is about 2.6 percent and should follow the static pressure radial profile (Fig. 4b).

The molecular constants of the two electronic states ( $A^1\Pi$  and  $X^1$ ), measured by several investigators and reported critically by Huber and Herzberg (Ref. 5), are given in Table 2. The values are for  $\text{Al}^{35}\text{Cl}$ , although  $\text{Al}^{37}\text{Cl}$  also naturally occurs. These two isotopes occur in a ratio of 75.5 to 24.5. The relatively small vibrational constant of the ground state ( $480\text{ cm}^{-1}$ ) leads to a vibrational-rotational fundamental at a wavelength of about  $21\text{ }\mu\text{m}$ . (Observation of this LWIR emission band from rocket plumes has not been reported.) The constants of the  $X^1\Sigma$  state have been re-measured recently in the infrared bands, and improvements in accuracy have been reported. These data will be introduced shortly. The rotational constants for this closely packed molecule are also quite small (approximately  $0.254\text{ cm}^{-1}$ ), and the overlapping branches make resolution of the lines nearly impossible. The vibrational correction to the rotational constant given as footnotes in Ref. 5 is a necessity for proper modeling of this band. Also, because of the small values of  $B_e$ , rotational quantum numbers out to at least 100 must be used at the temperature of interest.

### 2.4 RADIATIVE TRANSFER MODEL

The preliminary model adopted for this study is illustrated in Fig. 5. It is supposed that the core of solid particulates provides a continuum source for transmission through a layer of gas containing the absorbing AlCl. The continuum radiation from the particulates was curve fit by joining the spectra at both extremes of the absorption feature, and served as a source for the absorption calculations. The gas layer was considered uniform for these

preliminary calculations, with temperature and number density as parameters. The absorption spectra were modeled as Voigt lines with the spectrometer triangular slit function considered to be much greater than a line width.

A complete solution to the monochromatic radiative transfer equation is desired. The equation is written

$$\frac{dI_\nu}{dx} = S_E N_{TOT} L_\nu - S_A N_{TOT} L_\nu I_\nu \quad (1)$$

where

$N_{TOT}$  = Total number density of emitter/absorber

$L_\nu$  = Line shape function

$S_E$  = Molecular emission strength

$S_A$  = Molecular absorption strength

$I_\nu$  = Spectral radiance (i.e.,  $W/sr\text{-}cm^2 \text{-} cm^{-1}$ ) at wavenumber  $\nu$

$x$  = Spatial coordinate within the media

The boundary condition at  $x = 0$  is given in this case by the fit to the continuum spectra, neglecting the AlCl absorption feature; i.e., the continuum background.

Conceptually, the calculation involves 3 steps:

1. Determine the positions of all spectral lines. Determine the AlCl emission and absorption strengths for each line based on a rotational and vibrational temperature. This yields a spectral line atlas of line strengths versus line center wavenumber for all lines.
2. Given  $S_A$  and  $S_E$ , and  $N_{TOT}$ , solve Eq. (1). Here, only one spatial zone is considered so that integration of Eq. (1) is simplified.
3. Convolve the result of step 2 for each line with spectrometer response function. In this case a triangular slit function suffices since the actual line width is much smaller than the instrument monochromatic response function.

## 2.4.1 Part 1

The strength of each emission line is given by

$$S_E = \frac{hc\nu}{4\pi} A_{v',v''} \frac{S_{J',J''}}{2J' + 1} \chi(A;v';J') \quad (2)$$

where

$A_{v',v''}$  = Einstein coefficients, (Ref. 7)

$S_{J',J''}$  = Honl-London factor (Ref. 8)

$\nu$  = Wavenumber

$\chi(A;v';J')$  = Fractional population of the  $A^1\Pi$  state for  $v'$  and  $J'$  level, normalized by the partition function, i.e.,

$$\chi(A,v',J') = \frac{g_{Av',J'} \exp \left[ - \frac{hc}{kT} E(A,v',J') \right]}{\sum_i g_i \exp \left[ - \frac{hc}{kT} E_i \right]} \quad (3)$$

where  $g_i$  is the degeneracy factor of the given state. The absorption strength is similarly given by

$$S_A = h\nu B_{v',v''} \frac{S_{J',J''}}{2J'' + 1} \{ \chi(X,v'',J'') - \chi(A,v',J') \} \quad (4)$$

with the Einstein B coefficient as

$$B_{v',v''} = \frac{1}{8\pi hc\nu^3} A_{v',v''} \quad (5)$$

The band strength (or lifetime) of the  $AlCl$   $A^1\Pi$   $\nu = 0$  state has been measured (Ref. 6) to be  $6.4 \times 10^{-9}$  sec, where no effort was made to separate the two isotopic states. The lifetime was calculated to be  $5.17 \times 10^{-9}$  sec by Langhoff and Bauschlicher (Ref. 7), who also calculated relative band strengths from first principles. The transition probabilities for each significant vibrational transition are given as Einstein coefficients in Table 3, where the calculated lifetime was used. Note the relatively strong values for the  $\Delta v = 0$  sequence,

indicating that these will be the most evident in the structure, as also reported in the experimental analyses (Ref. 3). These calculations of band transition probabilities were made for  $\text{Al}^{35}\text{Cl}$ , with the assumption that the results are the same for  $\text{Al}^{37}\text{Cl}$ .

Energies of individual states are given by

$$E_i = T_i = E_{v_i} + E_{R_i} \quad (6)$$

where  $T_i$  is electronic state energy,  $E_{v_i}$  is the vibrational state energy, and  $E_{R_i}$  is the rotational energy of quantum. Now, in terms of the vibrational quantum number  $v$ , the rotational quantum number  $J$ , and the electronic angular momentum quantum number  $\Lambda$ ,

$$E_{v_i} = \omega_e (v + 1/2) - \omega_e x_e (v + 1/2)^2 + \omega_e y_e (v + 1/2)^3 \quad (7)$$

$$E_{R_i} = B_v [J(J + 1) - \Lambda^2] - D_v [(J(J + 1) - \Lambda^2)^2] \quad (8)$$

with

$$B_v = B_e \alpha_e (v + 1/2) + \alpha'_e (v + 1/2)^2 + \alpha''_e (v + 1/2)^3$$

$$D_v = D_e + \beta_e (v + 1/2)$$

For mass  $\text{Al}^{37}\text{Cl}$ , all constants are modified by the ratio  $\rho = \sqrt{35/37}$

$$B_e^{(37)} = B_e^{(35)} \rho^2$$

$$\alpha_e^{(37)} = \alpha_e^{(35)} \rho^3 \text{ etc.}$$

The molecular constants for the  $A^1\Pi$  state were taken from Huber and Herzberg (Ref. 5) and are listed in Table 2. For the ground electronic state, Bernath's measurements use the Dunham expression (Ref. 8) for the sum of the vibrational and rotational energy,

$$T_{vJ} = \sum_{l,m} Y_{lm} (v + 1/2)^l [J(J + 1)]^m \quad (9)$$

The values of  $Y_{lm}$  were given to the authors by Bernath and appear in Table 4. With the transition energies defined, line positions are obtained by subtraction

$$v = E(A, v', J') - E(X, v'', J'')$$

A line atlas is built up from these expression for  $v'$ ,  $v''$  out to 8 and  $J'$ ,  $J''$  out to 200 for both isotopes.

### 2.4.2 Part 2

The line-by-line model then solves Eq. (1) for each line in the atlas. A Voigt profile for each line is assumed. The  $S_E$  and  $S_A$  are calculated at a minimum of ten spectral frequencies between spectral line centers by summing contributions of all relevant lines at that position. Here  $v', v''$  out to 8 and  $J', J''$  out to 200 are used to generate a large number of stored numbers. Thus, for 20,000 spectral lines, at least 200,000 radiances and transmittances are generated. The program also does spatial integration, although for this case (1 zone) the integration is trivial.

### 2.4.3 Part 3

The spectrometer is modeled by a triangle function of  $2\text{\AA}$  full width at half maximum. The convolution of the integral

$$H(\nu) = \int I(\nu - \nu') G(\nu') d\nu' \quad (10)$$

is done numerically using the trapezoid rule, where  $H(\nu)$  represents the instrument reading at  $\nu$  and  $G(\nu')$  represents the instrument function,

## 2.5 MODELING RESULTS

The approach taken was to vary the vibrational and rotational temperatures, the column density, and the column length in Eq. (2) until the closest fit to the experimental data was achieved. The temperature and pressure were varied about the predicted averages along the column, (see Fig. 4) and the predicted mole fraction of  $\text{AlCl}$  was used initially. It was first necessary to calculate the constants accurately for each vibrational state of each of the isotopic molecules. This proved to be very sensitive in obtaining a fit to the vibrational bandheads. Then, the number of  $J$  values necessary to fit the absorption level was determined.

Only two results will be shown: First, the result using the predicted temperature and  $\text{AlCl}$  density (Fig. 6) and the final result, the best fit (Fig. 7). As shown in Figs. 4 and 5, the parameters used for the baseline calculations were

Vibrational Temperature,  $T_v = 800 \text{ K}$

Rotational Temperature,  $T_r = 800 \text{ K}$

Number Density,  $\eta = 2.36 \times 10^{16} \text{ cm}^{-3}$

Absorber Path Length,  $\ell = 5 \text{ cm}$

Quite clearly from Fig. 6, the fit of the calculation to the data is poor. The structure is much smoother than the data, although the same spectral resolution was used in the model as for the spectrometer. In the process of iterating on temperature and density, a better fit could be found in the central portion of the absorption, but the structure in the wings became poorer. It was this lack of spectral fit that led to use of the more accurate data for the  $X^1\Sigma$  state. Finally, since the molecular data for the upper state are somewhat dated and some uncertainty exists in the relative values of the rotational constant for the two isotopes, the vibrational and rotational constants of the  $A^1\Pi$  state were also iterated. Since this process could go on and on, a final fit (Fig. 7) was produced. The final parameters are as follows:

Vibrational Temperature,  $T_v = 1,000$  K

Rotational Temperature,  $T_r = 1,000$  K

Number Density,  $\eta = 2.36 \times 10^{16} \text{ cm}^{-3}$

Absorber Path Length,  $\ell = 5$  cm

and the molecular constants were also shifted:

$\omega_e 450 \rightarrow 430 \text{ cm}^{-1}$

$\omega_e x_e 4.3 \rightarrow 4.1 \text{ cm}^{-1}$

$B_e 0.259 \rightarrow 0.249 \text{ cm}^{-1}$

Here, the spectral match is fair and the overall absorption matches pretty well, so that continued iteration appears unwarranted.

The final result is reasonable. Because of the high particle temperature, it is not surprising to have a gas temperature somewhat larger than predicted (1,000 K versus 800 K predicted). Also, because of small particles in the outer gas flow, it is not surprising that the radiation from the gas layer masks the absorption at the deepest absorption frequency. One might expect that an arbitrary shift of the wavelength for the experimental data would produce a better fit. However, attempts to make this match were only marginally successful. The simple physical model of Fig. 5 cannot be correct, since the radiation is obviously extended and the  $\text{AlCl}$  exists all through the plume. However, the modeling brought assurance that the absorber was  $\text{AlCl}$ , and only a slight variation of temperature brought the model results very near the measured data.

## 2.6 CONCLUSIONS

Clearly, if the AlCl feature is to be used for diagnostics, laboratory work using a heated absorption cell will be required to reach a better fit between calculated and measured spectra. In a heated cell experiment the temperature and pressure parameters would be well known, leaving only the spectrometer wavelength calibration and the molecular constants unknown. The issues raised above can then be resolved.

## 3.0 SEARCHLIGHT EMISSION ANALYSIS

### 3.1 INTRODUCTION

Prediction of plume radiative heat transfer to spacecraft is important for the design of vehicle thermal protection systems. Radiative heating is of particular concern for aluminized solid-propellant rocket motors because of the intense thermal continuum emission from their exhaust plumes. The continuum is largely due to thermal emission from hot micron-sized aluminum oxide droplets and particles in the exhaust plume with temperatures in the range 2,000 - 2,500 K. Because of uncertainties in  $\text{Al}_2\text{O}_3$  size, temperature, and emissivity, *a priori* code predictions are unreliable. Spacecraft designers have instead relied on empirical methods to predict in-flight heat transfer. This works well for launch vehicles because it is usually possible in a ground test to measure the heat flux in the desired locations and viewing angles.

The situation is different for space motors, however, because these are tested in altitude simulation facilities with close proximity to an exhaust diffuser duct. It is almost never possible to observe more than a meter or so of undisturbed plume flow. Sometimes only a few inches of plume are visible. In addition, the diffuser restricts the achievable viewing angles to near 90 deg, broadside to the plume. The viewing angles important for spacecraft heating, by comparison, are nearer to 30 deg. One is, therefore, left with the problem of reconstructing the radiative heat flux from this limited database. Bobco (Ref. 9) and Edwards (Refs. 10-12) describe the current industry standard method for curve fitting plume data from altitude tests in which the axial decay in radiosity is measured, to a radiative exchange view factor model. The principal difficulty in applying this method is the need to extrapolate the full spatial and aspect angle dependences of the plume radiance based on a limited number of radiometer or IR camera measurements, all of which are necessarily limited to the nozzle exit region and to roughly 90-deg aspect angle.

Recent measurements of several motors at the AEDC (Ref. 13) suggest that a significant portion of the broadside exit plane radiance of space motors may be due to nozzle searchlight emission. Specifically, the broadside radiance near the nozzle exit plane appears to contain significant contributions from the hot inner nozzle wall. Although not directly in the line

of sight, the intense nozzle radiation is scattered into the field of view by  $\text{Al}_2\text{O}_3$  droplets and particles in the plume (Fig. 8). There has, therefore, been great interest in understanding both the strength of this searchlight emission and its implications for in-flight heat transfer. This is not easy, as radiometers and IR cameras cannot *per se* distinguish between searchlight and direct plume emission. Instead, the identification of searchlight emission must be made on the basis of characteristic temporal, wavelength, and spatial properties of the radiance data. The following sections indicate what some of these characteristic properties of searchlight emission are and how they occur in selected motor test data.

### 3.2 SEARCHLIGHT MECHANISM

This section describes the radiative transport properties in rocket exhaust plumes and shows why these should naturally lead to a strong searchlight effect. To dispel possible confusion, it should first be mentioned that the term "searchlight" is a misnomer. It was originally proposed on the mistaken assumption that the radiation in question originated from the extremely hot combustion chamber (Ref. 14). Additionally, the word "searchlight" implies a degree of collimation which simply does not occur in rockets. Since it has become entrenched in the technical jargon, however, we continue to use it in this report.

The searchlight mechanism is a light-scattering process controlled by the radiative transport properties of the plume. The scattering is due to micron-sized  $\text{Al}_2\text{O}_3$  particulates which typically comprise 30 percent of the mass flow. Since the particulate temperatures bracket the material melt point of 2,327 K, both solid particles and liquid droplets occur. Figure 9 shows that these particles are very efficient scatterers of infrared radiation. Specifically, this figure shows the Mie scattering albedo of a representative 3- $\mu\text{m}$ -radius liquid  $\text{Al}_2\text{O}_3$  droplet between 1- and 4- $\mu\text{m}$  wavelength. It was generated using the BHMIE code of Ref. 15 and the real refractive index data of Refs. 16-19. The spectral structure is due to Mie resonances and would be smoothed out for a distribution of particle sizes. As can be seen, the albedo is close to 99 percent over this entire spectral region. It would be even higher for a solid particle. The directional properties of this scattering are indicated in Fig. 10, which shows the normalized scattering phase functions for the same 3- $\mu\text{m}$ -radius droplet at 1-, 2-, and 3- $\mu\text{m}$  wavelength. The scattering efficiency is highest in the forward direction (0 deg) and drops rapidly with increasing angle. The inset indicates how this directionality affects the intensity of searchlight emission at different aspect angles. It considers emission from the nozzle wall which is scattered at a plume volume element  $dV$ . The ray path labeled A contributes to the broadside radiance. Since the scattering angle is small, the efficiency is high. Path B contributes to vehicle heating. Since the scattering angle is large, the efficiency is low. Based upon this reasoning, the searchlight is expected to contribute more strongly to broadside radiance than to spacecraft heating.



In addition to the scattering properties of single particles, searchlight is also affected by the aggregate transport properties of the total plume. The two important parameters in this regard are the scattering and the absorption optical depths,  $\tau_s$  and  $\tau_a$ , respectively. An estimate of these parameters can be made using the data of Fig. 9, the nominal particle size given by the Hermesen size correlation (Ref. 20), and assuming one-dimensional source flow as indicated in Refs. 21-23.

$$\frac{\tau_s}{Q_s} = \frac{\tau_a}{Q_a} = \frac{3 m}{2\pi \rho R v} (1.38 E - 4 D_t^{0.3})^{-1} \quad (11)$$

where

$Q_a$  = Mie absorption efficiency parameter

$Q_s$  = Mie scattering efficiency parameter

$D_t$  = Nozzle throat diameter

$m$  =  $\text{Al}_2\text{O}_3$  mass flow rate

$R$  = Plume radius

$\rho$  = Bulk density of  $\text{Al}_2\text{O}_3$

$v$  = Particle velocity

All parameters are in cgs units. For small to mid-sized motors, the predicted scattering optical depth is on the order of unity or larger (i.e., optically thick). This means that most photons propagated along a diameter through the plume will be scattered at least once and possibly several times. The absorption optical depth, on the other hand, is only several percent (i.e., optically thin). This means that radiation can propagate through the plume without appreciable absorption. Another consequence of the low absorption optical depth is that the plume emission will tend to scale linearly with thrust.

A simple gedanken experiment further clarifies both the strength and spatial dependence of the searchlight. Consider a single alumina droplet suspended over a hot, flat plate with unit emissivity (Fig. 11). The droplet both emits radiation and scatters radiation from the plate. One then observes the total droplet radiance along a line of sight parallel to the surface

of the plate and which at no time views the plate directly. If the height of the droplet above the plate  $z$  is much smaller than the size of the plate  $L$ , the plate appears essentially infinite. The thermal emission from the droplet is

$$\pi r^2 Q_a B(T_d) \quad (12)$$

where

$r$  = Droplet radius

$Q_a$  = Mie absorption efficiency parameter

$B$  = Planck radiation function

$T_d$  = Droplet temperature

The radiation emitted by the plate and scattered into the line of sight ( $\hat{x}$  direction) by the droplet is the searchlight emission. It is given by

$$\pi r^2 Q_s B(T_p) \int P(\Omega - \hat{x}) d\Omega \quad (13)$$

where

$Q_s$  = Mie scattering efficiency parameter

$P$  = Scattering phase function normalized to unity over  $4\pi$  steradians

$T_p$  = Temperature of the plate

$\Omega$  = Angular coordinate

Because  $z \ll L$ , the flat plate occupies one hemisphere, and the angular integral in Eq.(13) is therefore also performed only over a hemisphere. By symmetry and the normalization condition on  $P$ , the integration of  $P$  over a hemisphere equals one-half. The radiance scattered into the line of sight is therefore

$$\frac{\pi r^2 Q_s}{2} B(T_p) \quad (14)$$

where  $T_p$  is the temperature of the flat plate. It is now instructive to substitute values appropriate to rocket plumes. We use

$$Q_a = 0.02,$$

$$Q_s = 1.98,$$

$$T_d = 2,300 \text{ K, and}$$

$$T_p = 1,300 \text{ K}$$

The latter is a representative adiabatic wall temperature at the nozzle lip. At a wavelength of  $1.5 \mu\text{m}$ , the scattered searchlight emission is twice the directly emitted radiance.

As the droplet is lifted higher above the plate, the searchlight emission decreases for two reasons. First, the plate no longer appears infinite. The scattering integral, Eq. (13), is limited to a smaller solid angle which approaches the asymptotic limit ( $L/z$ , Ref. 2) (i.e., inverse square law) for large  $z$ . This is simply the radiative exchange view factor between a flat plate and a distant point. Second, the scattering angles all approach a limiting value of  $90^\circ$ . The asymptotic limit of the searchlight term is therefore

$$\pi^2 Q_s P(90^\circ) B(T_p) \left(\frac{L}{z}\right)^2 \quad (15)$$

### 3.3 PLUME RADIATION MEASUREMENTS

Selected radiometer and calorimeter data from two motors are reviewed to illustrate some of the recurrent features of exhaust plumes observed at the AEDC altitude simulation test chambers. These data were obtained on targets of opportunity on a noninterference basis during routine motor qualification and testing. They are not a complete set, and at no time was it possible to perform a dedicated, comprehensive measurements set on any single motor. However, the available data exhibit characteristic spatial, temporal, and wavelength trends which indicate strong searchlight emission at the nozzle exit plane.

Even for small motors, the exit plane radiance does not scale linearly with thrust. Instead, it tends to increase more slowly than thrust after ignition and then to continue climbing during the late burn, sometimes even after the thrust is level or tailing off. Figure 12 shows the radiance 2 in. downstream of the nozzle exit plane measured by a narrow-field-of-view calorimeter at  $90^\circ$  aspect angle for motor A. Although the thrust peaks at 35 sec, the radiation does not peak until 65 sec. In addition, the initial overshoot in thrust near 10 sec is not accompanied

by a corresponding feature in the radiance. In many cases there are no further data from a motor firing, and the cause of such nonlinearity remains unknown. For this particular motor, however, calorimeter time histories were also measured at two additional downstream locations (Fig. 13). Although all three calorimeters were aimed at the centerline, the profiles are strikingly different. In particular, as one progresses downstream, they gradually become more like the thrust curve. This is consistent with a localized searchlight enhancement of exit plane radiation, but is not conclusive. The spikes in the data for all three channels are attributed to the repeated ejection alumina slag from the motor and were also evident in the video as bright flashes.

Spectrometer data provide another important test of the searchlight mechanism. In the long wavelength infrared (LWIR), the exhaust particles are inefficient scatterers (Refs. 16 and 17), and strong searchlight scattering cannot occur. If the searchlight hypothesis is correct, then little or no excess radiation should appear in the far infrared. Figure 14 confirms this for motor B. This figure was generated from 2- to 14- $\mu\text{m}$  exit plane spectra with a scan time of approximately 2 sec per spectrum. It compares the time histories of the short wavelength infrared (SWIR) and LWIR emission against motor thrust. The data have been normalized at the second time point. Whereas the LWIR band tracks the thrust quite closely, the SWIR band deviates from it as it did for motor A. This result indicates that the anomalous exit plane radiance profiles are associated with scattering from exhaust  $\text{Al}_2\text{O}_3$  in the plume. In addition, the close correspondence of the LWIR and thrust profiles indicates that the flow-field and particle properties remain fairly steady over the course of the burn. This same measurement was unsuccessfully attempted on a larger motor. The plume was opaque and the LWIR radiance profile was flat, except during ignition and tailoff. This is consistent with the high LWIR emissivity of  $\text{Al}_2\text{O}_3$ . The dual-wavelength method is, therefore, useful only for small motors.

Additional information was sought in the response of the SWIR radiance to fluctuations in thrust. The fluctuations under consideration are fairly slow and arise from normal chamber pressure excursions as the area of the burning propellant grain changes. The bump in the thrust profile of motor A near 10 sec in Fig. 12 is a good example. Since the plume is optically thin with respect to absorption, the direct emission from the plume should respond almost instantly (within milliseconds) and, at least to first approximation, linearly to thrust changes. As can be seen, however, this is not the case.

To better quantify this observation, the thrust and radiance data of Fig. 12 were Fourier transformed into the frequency domain (Fig. 15). The quantity of interest is not the particular shape of the transforms, but rather their ratio, as this gives the frequency response function of the SWIR to thrust. If all of the radiance were due to direct plume emission, the response function would be flat, and the two curves would overlay each other. What actually occurs is that the radiance power spectral density begins to fall below the thrust curve above roughly

0.2 Hz. The searchlight hypothesis affords a natural explanation for this in terms of the thermal lag time of the nozzle. Specifically, above approximately 0.2 Hz the fluctuations are too fast for the nozzle temperature to track, and only the direct plume emission contributes to the radiance fluctuations. Nozzle thermal lag also provides a reasonable explanation for the way in which the SWIR initially lags behind the thrust.

In the case of motor B, a calculated nozzle lip radiance time history  $B(t)$  was available (Fig. 16). The predicted intensity is several times that of the plume. This indicates that the efficiency of the searchlight scattering mechanism does not need to be very high to account for the data. In addition, the calculation shows that the thermal lag time of the nozzle lip is consistent with the observed lag times of exit plane radiance. An attempt was made to see how well the observed SWIR time history could be explained using a linear sum of two functions, one proportional to the thrust (the direct plume emission), and the other to the calculated nozzle radiance (the searchlight emission). This neglects changes in the searchlight scattering properties of the plume with thrust and so is only approximate. A least-squares fit to the two components gave the results of Fig. 17. The overall profile of the SWIR data was fairly well described by this procedure. However, the inferred intensity of the searchlight emission was more than twice as great as that indicated by the SWIR versus LWIR comparison shown previously in Fig. 14. Since the nozzle radiance calculations suffer from uncertainty in the high-temperature properties of the partially pyrolyzed carbon phenolic nozzle material, the SWIR versus LWIR comparison is probably more reliable.

### 3.4 MONTE CARLO ESTIMATE OF SEARCHLIGHT INTENSITY

A theoretical basis for the preceding observations can be established using the Monte Carlo method for radiative transport. This method provides a means of assessing realistic plume effects such as multiple scattering and inhomogeneity. For the present application, the backward Monte Carlo method, sometimes called time-reversed Monte Carlo, is computationally much more efficient. In this variant, one computes absorption rather than emission. By Kirchoff's law, the two are equal under conditions of local thermodynamic equilibrium. Absorption probabilities are estimated by ray tracing photons with small, randomized step size through the plume. The probability of absorption and scattering within each step is determined using a random number generator. If scattering occurs, a new random direction is chosen consistent with scattering phase function. The ray trace is continued until the photon is either absorbed or escapes from the plume boundary. Monte Carlo calculations for the emissivity of anisotropic scattering slabs agreed with numerical results (Ref. 24) to within the expected standard deviation. This was about one percent for  $10^4$  photons.

The Monte Carlo searchlight calculation requires specification of the spatial distribution of particles within the plume. The radial distribution of particles for motor A was based

upon Abel inversion of Nd:YAG laser transmission measurements performed at eight radial locations (Fig. 18). The quantity determined by this measurement is the extinction coefficient and is used directly by the Monte Carlo code. Several inversions performed approximately 1 sec apart are shown for two time segments, one near the beginning and one near the end of the motor burn. Successive inversions are shown to give repeatable results. The differences in the profiles at the beginning and end of the burn are attributed to differences in chamber pressure and the internal grain configuration. The depletion of the particle extinction at the plume centerline is not due to spin, as the motor was stationary. The highly nonuniform nature of this distribution indicates the value of IR camera measurements. The particle distribution at other axial locations was scaled from these results assuming a conical expansion.

The scattering phase function was approximated by the Henyey-Greenstein function (Refs. 25 and 26). This is an analytical approximation to the Mie scattering phase function. It lacks the backscatter lobe near 180 deg, but it is otherwise a good representation of the full Mie result, especially if one considers a distribution of droplet sizes. The one free parameter of this function specifies the degree of forward scattering, specifically the mean cosine of the scattering angle. The value of this mean angle was taken to be 0.5, based on the size determined from a laser transmissometer and Mie calculations. The results were not sensitive to the precise value of this parameter. The volume scattering albedo and scattering phase function were assumed constant throughout the plume. As for the former, the actual value is sufficiently close to unity that small variations do not affect the basic scattering behavior of the plume. As for the latter, there is inadequate information to make a more detailed choice.

In the backward Monte Carlo method, the searchlight emission,  $I$ , is given by the product of the probability of absorption on the nozzle inner wall,  $dP/dz$ , times the intensity of emission at this point,  $B(z)$ . Because the nozzle is black carbon phenolic, this emission was taken to be the Planck function,  $B$ , at the wall surface temperature.

$$I = \int B(z) \frac{dP}{dz} dz \quad (16)$$

The quantity  $dP/dz$  can also be regarded as the differential view factor between the radiometer and the inner nozzle wall. The region of integration is from the nozzle exit to the throat. If the nozzle wall temperature is assumed constant over the region of integration, then the Planck function can be taken outside the integral. The searchlight can then be characterized by a view factor,  $F$ .

$$F = \int \frac{dP}{dz} dz \quad (17)$$

Two different normalizations for view factor are in common use. The one used here is  $\Sigma F_i = 1$ .

The probability distributions,  $dP/dz$ , for each of the three broadside radiometers used on motor A were determined from Monte Carlo histograms of 100,000 photons each with a bin size of 3 cm in the axial direction (Fig. 19). Each distribution contains a delta function component, due to directly transmitted photons, and a continuous bell-shaped component due to scattered photons. The directly transmitted component increases downstream because plume expansion reduces the overall scattering losses. Paths terminating to the left of the nozzle exit plane (at 0 cm) terminate on the inner nozzle wall and therefore contribute to searchlight emission. The integrals of the curves to the left of the exit plane give the searchlight view factors [Eq. (17)]. It is quite high, 0.33, at the 2-in. location. This is 2/3 of the theoretical maximum value of 0.5 at the exit plane. It then drops rapidly to 0.10 and 0.04 at the 17- and 29-in. stations, respectively. Comparison with the radiometer data of Fig. 13 indicates that this axial falloff is consistent with the data trend. As shown, most of the searchlight emission is predicted to originate primarily from the lip region of the nozzle. This is consistent with the fairly slow rise time of the excess radiation and justifies the use of a net view factor to characterize the searchlight.

The implications of searchlight emission for radiative heating were briefly alluded to in conjunction with Fig. 10, which indicated that the forward scattering nature of the plume particulates would tend to minimize searchlight emission in the direction of the vehicle. This issue is pursued further in Fig. 20, which shows the aspect angle dependence of the searchlight view factor for motor A. The view factors are computed for an exit plane calorimeter aimed at the plume centerline. The method and flow-field inputs are identical to those used for Fig. 19. Between 90 deg, where data were taken, and 30 deg, which is more relevant to vehicle heating, the searchlight drops by a factor of five. Even with multiple scattering, the searchlight does not contribute appreciably to vehicle heating. Heating rates based solely on broadside measurements will therefore be overly conservative. For critical applications, and certainly when the broadside searchlight is strong, a more realistic heating estimate will result if the searchlight component can be identified and removed by subtraction. There is a second and perhaps more important reason for subtracting the searchlight term. In the current industry standard method, the radiance of the downstream plume is extrapolated from a curve fit to the near-field (broadside) data. As has been shown, however, the spatial profile of the near-field plume radiance can be confounded by searchlight emission. In particular, if the searchlight emission is strong, then a curve fit to the near-field radiance profile may have only limited relevance to the direct plume thermal emission which one actually needs for heat transfer. Since the searchlight has a fast axial decay rate, moreover, a curve fit made without allowances for searchlight will tend to underestimate the radiance of the far-field plume.

### 3.5 SUMMARY

The prediction of in-flight radiative heat transfer from the plumes of aluminized solid-propellant space motors is difficult because typical altitude test facilities do not permit direct measurements of the heat flux at the desired locations and viewing angles. Instead, the in-flight heating must generally be extrapolated from a limited data set taken near the nozzle exit plane and basically broadside to the plume. Measurements of exhaust plume radiation from aluminized solid-propellant motors at the AEDC altitude test facilities indicate that both the intensity and spatial distribution of this radiation are confounded by searchlight emission. The broadside exit plane radiance does not scale with thrust, even for small motors. Instead, it lags behind the thrust curve after ignition and later continues to rise even when the thrust is level or tailing off. The radiance rise time is several seconds and is comparable to the calculated heating rate for the nozzle lip. At downstream locations, on the other hand, the radiance tends to track the thrust curve more closely. The anomalous exit plane radiance profile occurs only in the SWIR where alumina is a strong scatterer and is indiscernible in the LWIR where it is a poor scatterer. Finally, examination of the radiance and thrust power spectral densities in the frequency domain indicates the presence of two distinct components, one which responds rapidly to thrust fluctuations, and the other which responds with a time constant of several seconds.

These observations are attributed to searchlight emission. Specifically, they are attributed to hot nozzle wall radiation which is scattered into the broadside direction by the exhaust alumina particulates. The strength and the axial falloff of the searchlight emission are supported by Monte Carlo radiative transfer calculations using the measured plume extinction profile. It is concluded that searchlight emission is much stronger than has been previously supposed. Although it contributes strongly to the broadside exit plane radiance, it is probably not important at the smaller aspect angles relevant to vehicle heating. A more realistic estimate of the near-field plume radiance will result if the searchlight component can be identified and subtracted from the broadside radiance data. In addition, an improved extrapolation of the far-field plume radiance will also result, allowing the industry standard method to produce more accurate estimates of heat flux. If these corrections can be performed, the current industry standard method should then provide accurate estimates of the in-flight radiative heating load. To this end, several techniques for the identification and quantification of searchlight emission were attempted. Of the methods tried thus far, the best indicator is probably comparison of the exit plane versus downstream radiance time histories. Comparison of the SWIR and LWIR time histories appears to be a useful alternative for small motors, for which the LWIR alumina absorption is optically thin. It has the additional advantage of being applicable even when only a small length of plume is visible. The increased opacity of large motor plumes prevents its application for these motors.



#### 4.0 SUMMARY

The analyses of the AlCl absorption feature and the searchlight effect observed in solid-propellant rocket plumes during chamber tests at simulated altitudes show that these phenomena are of particular interest in the characterization of plumes. The AlCl absorption analysis indicates that this feature may be of use for plume diagnostics, although additional data are required before a better fit between calculated and measured spectra can be obtained (Ref. 27). The searchlight analysis indicates that searchlight emission is a strong component in the near-field plume and needs to be taken into account when attempting to extrapolate far-field plume radiance from near-field measurements (Ref. 28).

#### REFERENCES

1. Kolb, C. E., Ryali, S. B., and Warmhoudt, J. C. "The Chemical Physics of Ultraviolet Rocket Plume Signatures." SPIE Technical Conference, Orlando, FL, April 1988.
2. Erdman, P. W. and Levin, D. A. , et al. "In-Situ Measurements of UV and VUV Radiation from a Rocket Plume and Re-entry Bow Shock." AIAA Paper No. 92-0124, January 1992.
3. Pearse, R. W. B. and Gaydon, A. G. *The Identification of Molecular Spectra*. Wiley, New York, 1950, p. 47.
4. Dash, S. M. and Pergament, H. S. "A Computational System for the Analysis of Mixing/Chemical/Shock Processes in Supersonic Internal and Exhaust Plume Flowfields." AIAA Paper No. 80-1255, July 1980.
5. Huber, K. P. and Herzberg, G. *Molecular Spectra and Molecular Structure*. Van Nostrand Reinhold, Ltd., New York, 1979.
6. Rogowski, D. F. and Fontijn, A. "The Radiative Lifetime of AlCl A<sup>1</sup>Π," *Chemical Physics Letters*, Vol. 137, No. 3, June 1987, p. 219.
7. Langhoff, S. R. and Bauschlicher, C. W. "Theoretical Studies of AlF, AlCl and AlBr." *Journal of Chemical Physics*, Vol. 88, No. 9, pp. 5715-5725.
8. Kovacs, I. *Rotational Structure in the Spectra of Diatomic Molecules*. Adam Hilger Ltd., London, 1969.

9. Bobco, R. P. "Radiation from Conical Surfaces with Nonuniform Radiosity." *AIAA Journal*, Vol. 4, March 1966, pp. 544-546.
10. Edwards, D. K. and Bobco, R. P. "Effect of Particle Size Distribution on the Radiosity of Solid Propellant Rocket Motor Plumes." AIAA Paper No. 81-1052, June 1981.
11. Edwards, D. K. and Babikian, D. S. "A Two-Particle Model for Rocket Plume Radiation." *AIAA Journal of Thermophysics and Heat Transfer*, Vol. 1, No. 1, Jan. 1987, pp. 13-20.
12. Edwards, D. K. and Babikian, D. S., "Radiation from a Nongray Scattering, Emitting, and Absorbing Solid Rocket Motor Plume." *AIAA Journal of Thermophysics and Heat Transfer*, Vol. 4, No. 4., Oct. 1990, pp. 446-453.
13. Beale, K. S., et al. "Diagnostic Measurements on an Aluminized Propellant Plume During Spin and Nonspin Testing." AEDC-TR-90-28 (AD-A232101), Arnold AFB, TN 37389.
14. Laderman, A. J. and Carlson, D. J. "Comment on 'Thermal Radiation from the Exhaust Plume of an Aluminized Composite Propellant Rocket'." *AIAA Journal of Spacecraft and Rockets*, Vol. 5, No. 2, Feb. 1968, pp. 239-240.
15. Bohren, C. F. and Huffman, D. R. "Absorption and Scattering of Light by Small Particles." Wiley Interscience, New York, 1983.
16. Gryvnak, D. A. and Burch, D. E. "Optical and Infrared Properties of  $\text{Al}_2\text{O}_3$  at Elevated Temperature." *Journal of the Optical Society of America*, Vol. 55, No. 6, 1965, pp. 625-629.
17. Toon, O. B., Pollack, J. B., and Khare, B. N. "The Optical Constants of Several Atmospheric Aerosol Species: Ammonium Sulphate, Aluminum Oxide, and Sodium Chloride." *Journal of Geophysical Research*, Vol. 81, No. 33, pp. 5733-5748.
18. Konopka, W. L., Reed, R. A., and Calia, V. S. "Measurements of Infrared Optical Properties of  $\text{Al}_2\text{O}_3$  Rocket Particles." AIAA Paper No. 83-1568, June 1983.
19. Krishnan, S., et al. "Refractive Index of Liquid Aluminum Oxide at  $0.6328 \mu\text{m}$ ." *Journal of the American Ceramic Society*, Vol. 74, No. 4, April 1991, pp. 881-883.
20. Hermesen, R. W. "Aluminum Oxide Particle Size for Solid Rocket Motor Performance Prediction." *AIAA Journal of Spacecraft and Rockets*, Vol. 18, No. 6, Nov.-Dec. 1981, pp. 483-490.

21. Dobbins, R. A. and Jizmagian, G. S. "Optical Scattering Cross Sections for Polydispersions of Dielectric Spheres." *Journal of the Optical Society of America*, Vol. 56, No. 10, Oct. 1966, pp. 1345-1350.
22. Dobbins, R. A. and Jizmagian, G. S. "Particle Size Measurements Based on Use of Mean Scattering Cross Sections." *Journal of the Optical Society of America*, Vol. 56, No. 10, Oct. 1966, pp. 1351-1354.
23. Murphy, P. J. "Determination of Mean Particle Size in a Two-Phase Flow Free-Jet." Ph.D. Dissertation, University of Tennessee, Aug. 1990.
24. Van de Hulst, H. C. *Multiple Light Scattering: Tables, Formulas, and Applications*. Academic Press, New York, 1980.
25. Kamiuto, K. "Study of the Henyey-Greenstein Approximation to Scattering Phase Functions." *Journal of Quantitative Spectroscopy and Radiative Transfer*, Vol. 37, No. 4, 1987, pp. 411-413.
26. Henyey, L. G. and Greenstein, J. L. *Astrophysical Journal*, Vol. 85, 1941, p. 70.
27. McGregor, W. K., et al. "The AlCl<sub>3</sub> Absorption Feature in Solid Rocket Plume Radiation." AIAA Paper No. 92-2917, July 1992.
28. Reed, R. A., et al. "The Effect of Searchlight Emission on Radiation from Solid Rocket Plumes." AIAA Paper No. 92-2918, July 1992.

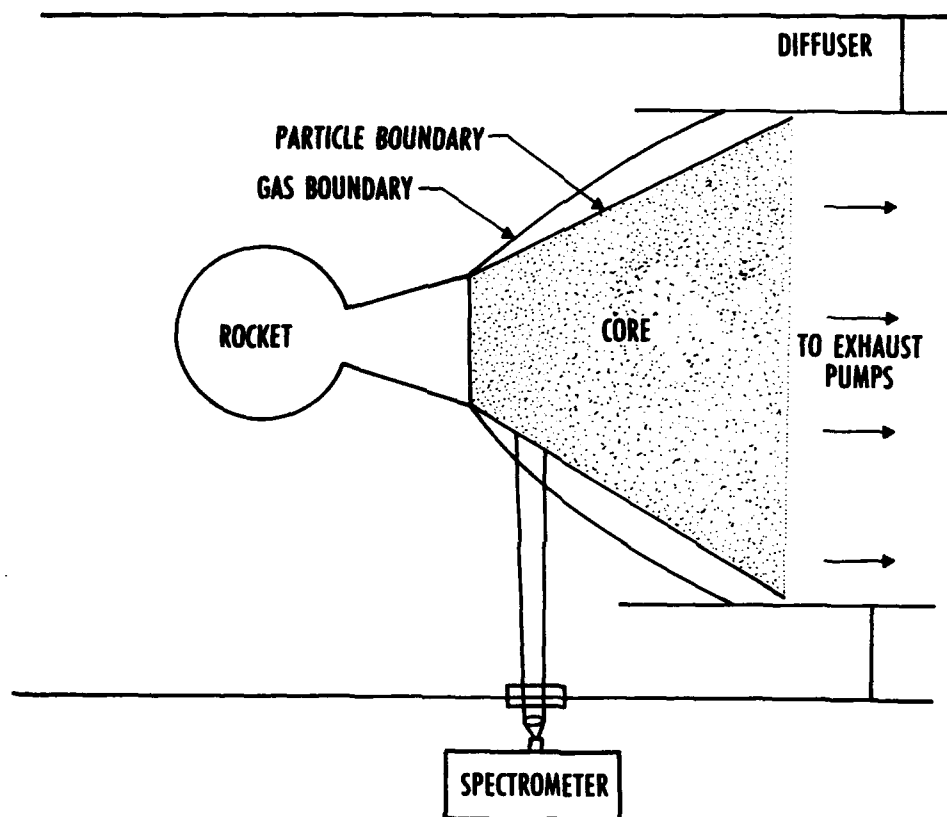


**Figure 1. Schematic of solid-propellant rocket motor test configuration used for UV spectral measurements.**

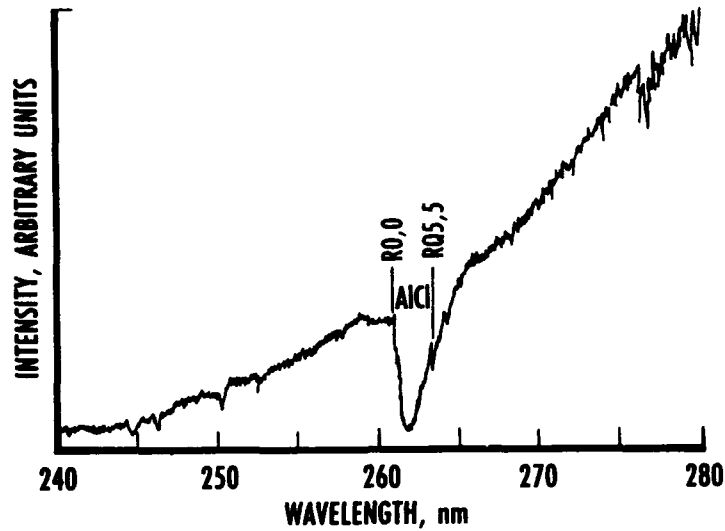


**Figure 2. Moderate-resolution mid-UV spectra from solid-propellant rocket motor plume.**

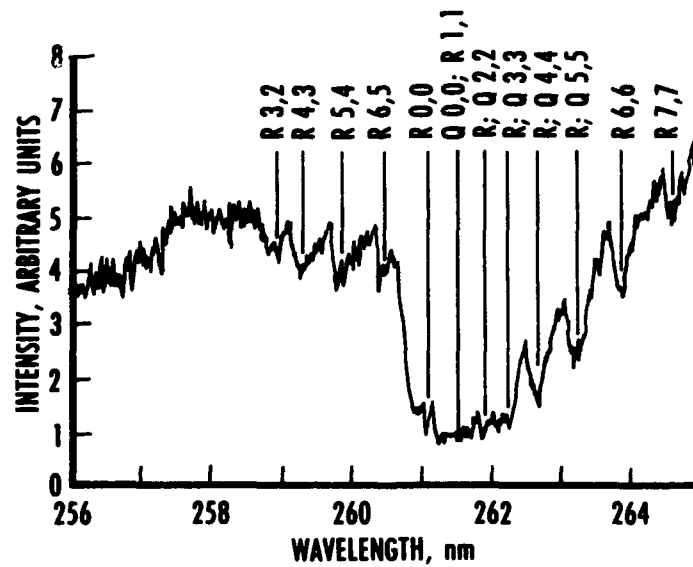
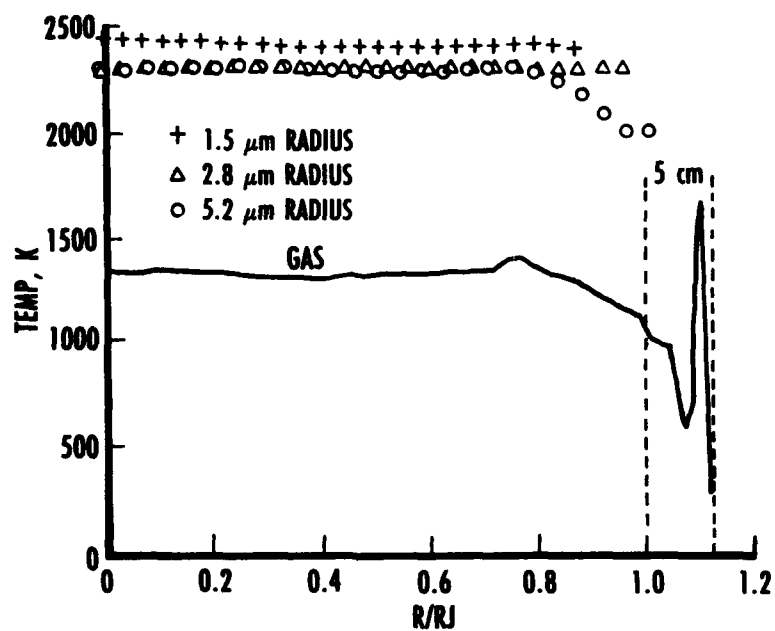
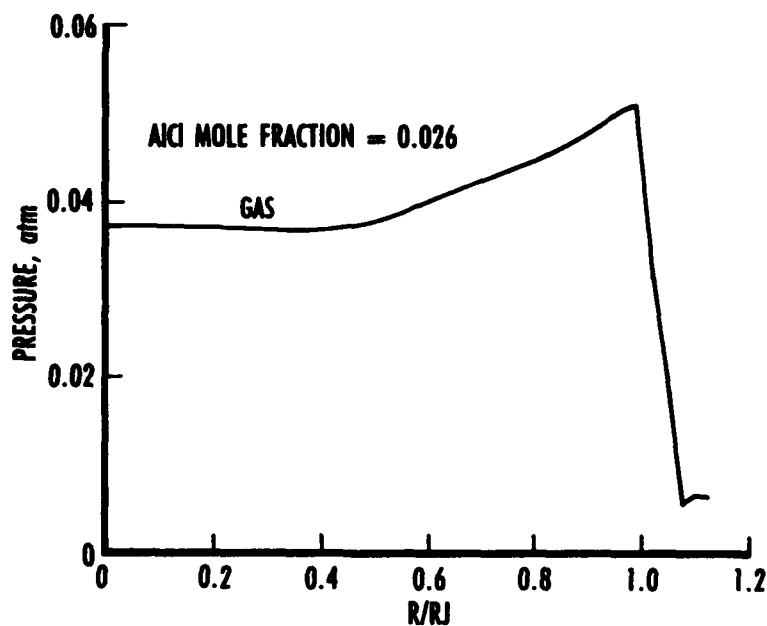


**Figure 3. High-resolution UV spectra from solid-propellant rocket motor plume.**



a. Temperature profile



b. Pressure profile

**Figure 4. Predicted radial profiles for solid-propellant rocket motor at axial location where UV spectra were measured (standard plume flow-field code using three particle groups).**

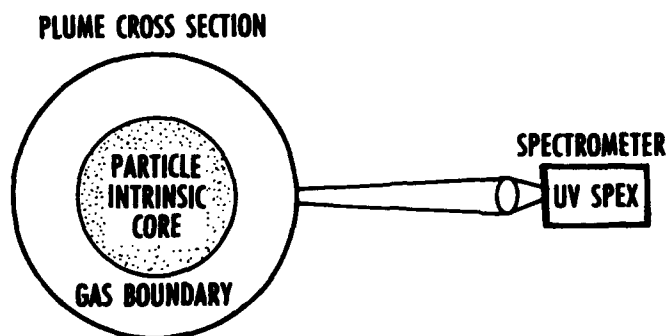


**Figure 5. Physical model of solid-propellant rocket motor plume UV spectral measurement experiment.**

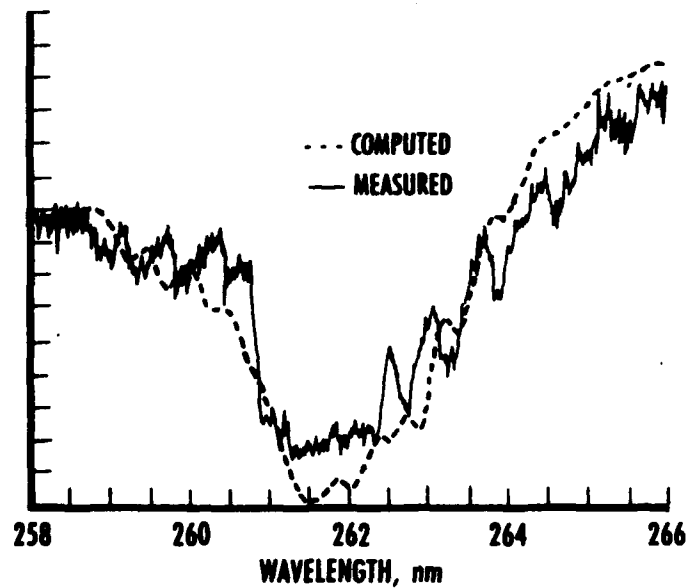


**Figure 6. Comparison of computed with measured spectra of SRM plume radiation at predicted plume conditions.**

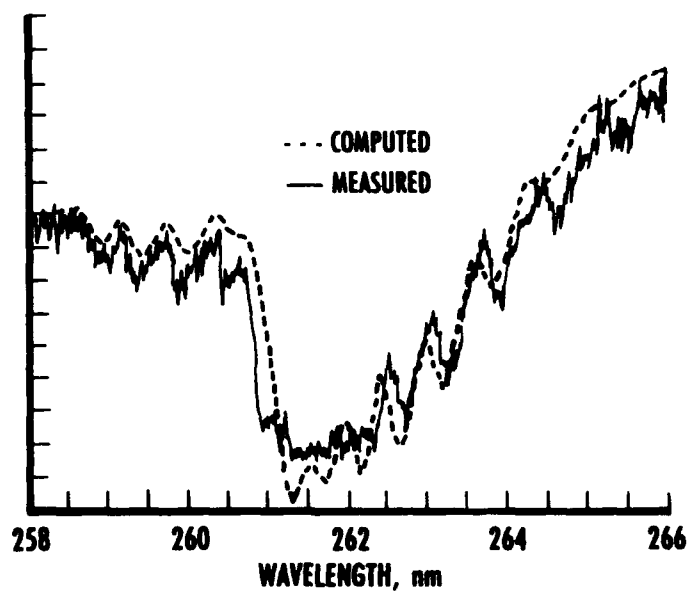


Figure 7. Comparison of computed with measured spectra of SRM plume radiation at "best fit" conditions.

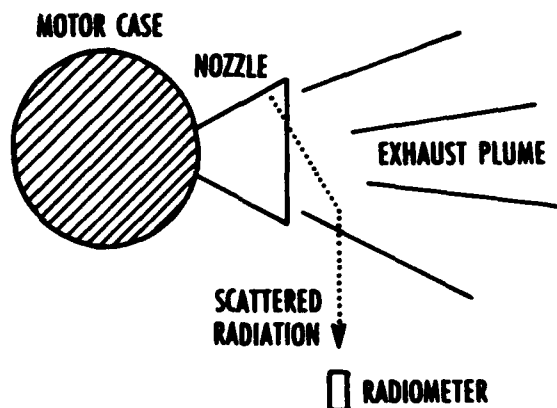


Figure 8. Sketch of searchlight emission where small angle scattering by plume  $\text{Al}_2\text{O}_3$  droplets and particles redirects nozzle emission toward broadside radiometers.



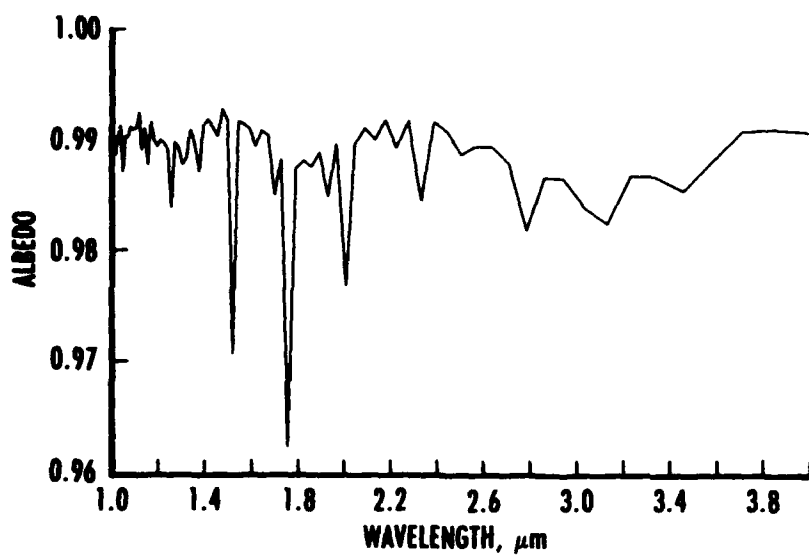


Figure 9. Mie scattering albedo of 3- $\mu\text{m}$ -radius  $\text{Al}_2\text{O}_3$  droplet.

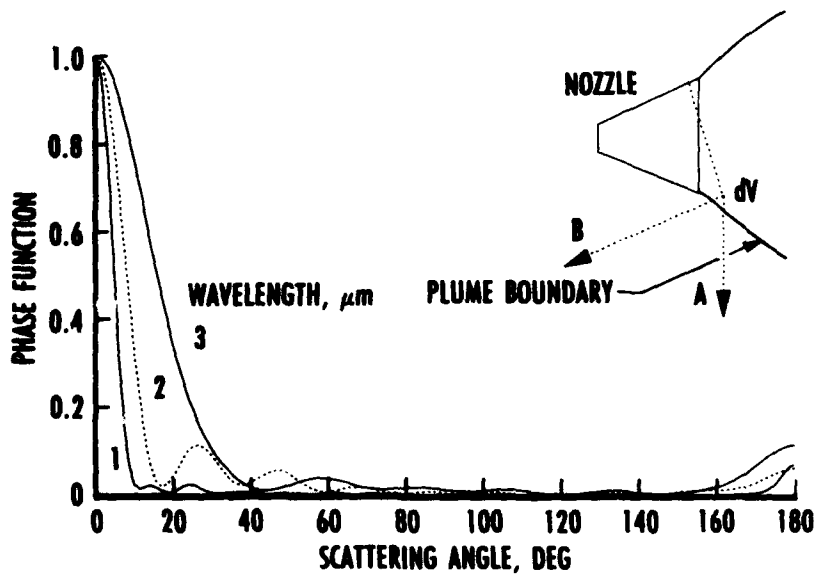
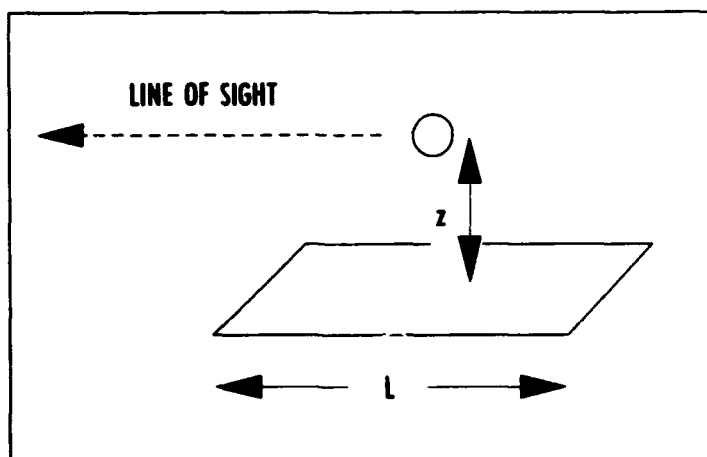
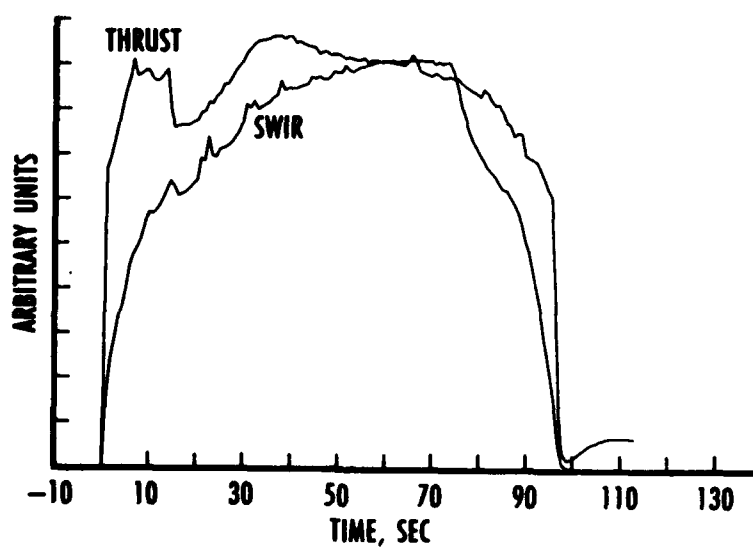


Figure 10. Scattering phase function of  $\text{Al}_2\text{O}_3$  droplet at three wavelengths.



**Figure 11. Geometry of gedanken experiment showing radiance of a reflecting and emitting sphere suspended above a hot plate.**



**Figure 12. Motor A thrust and SWIR radiance time histories.**

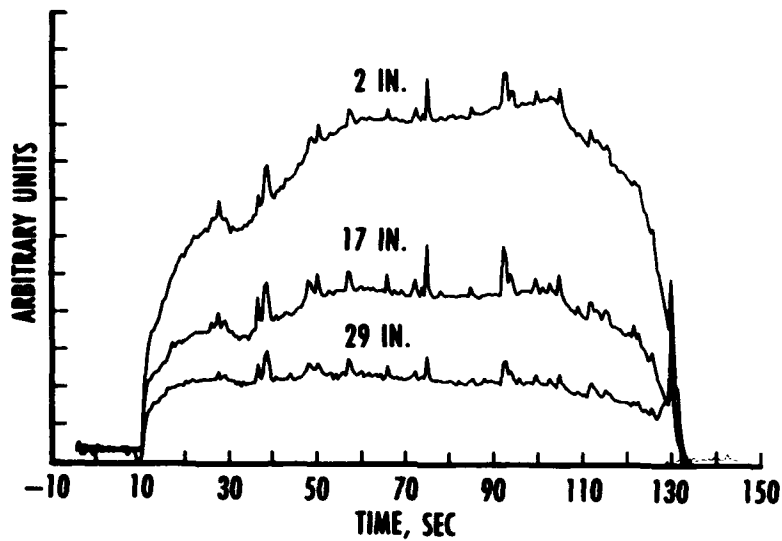


Figure 13. Radiative heat flux at three locations for motor A.

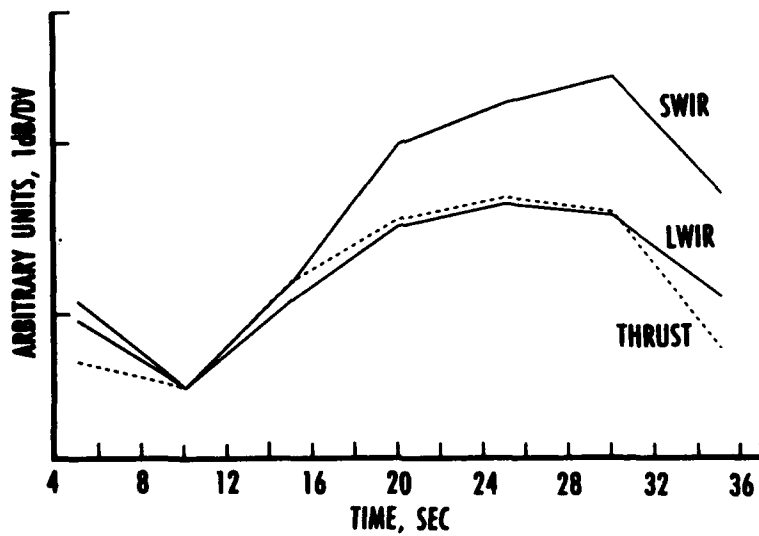


Figure 14. Normalized thrust, SWIR, and LWIR time histories for motor B.

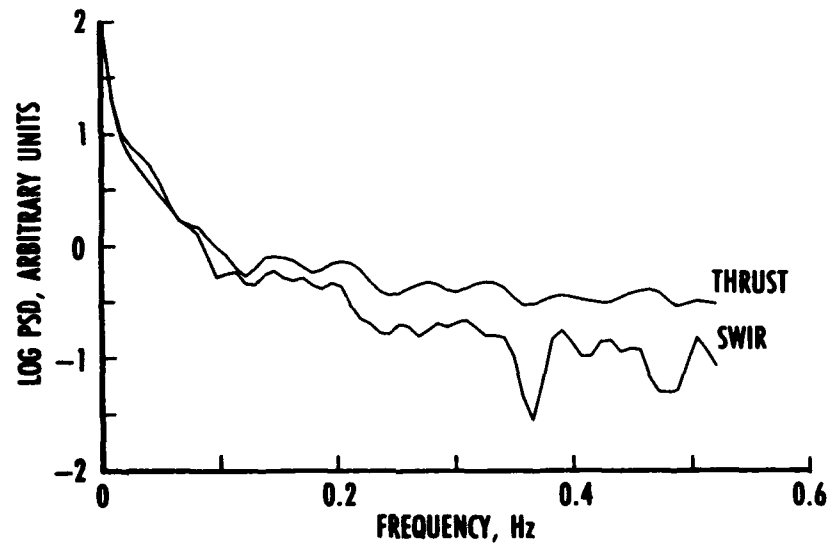


Figure 15. Power spectral density comparison of thrust versus short wavelength infrared (SWIR) radiance.

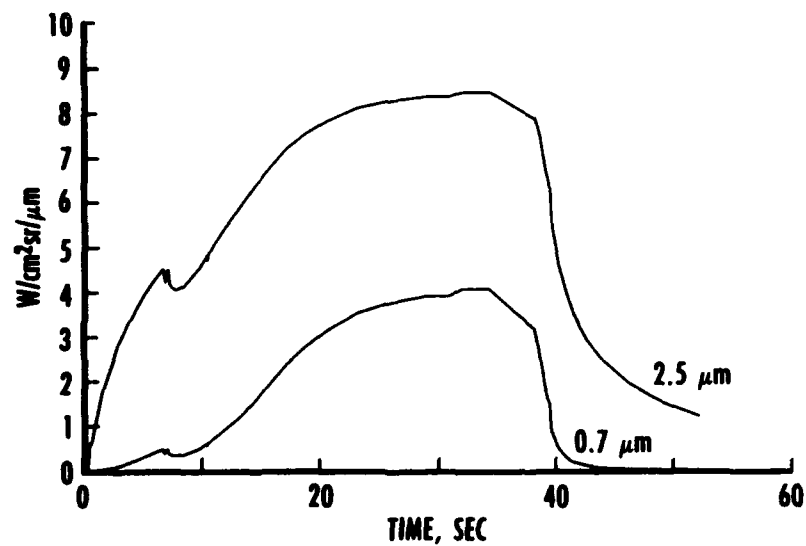


Figure 16. Calculated radiance of motor B nozzle lip at two wavelengths.

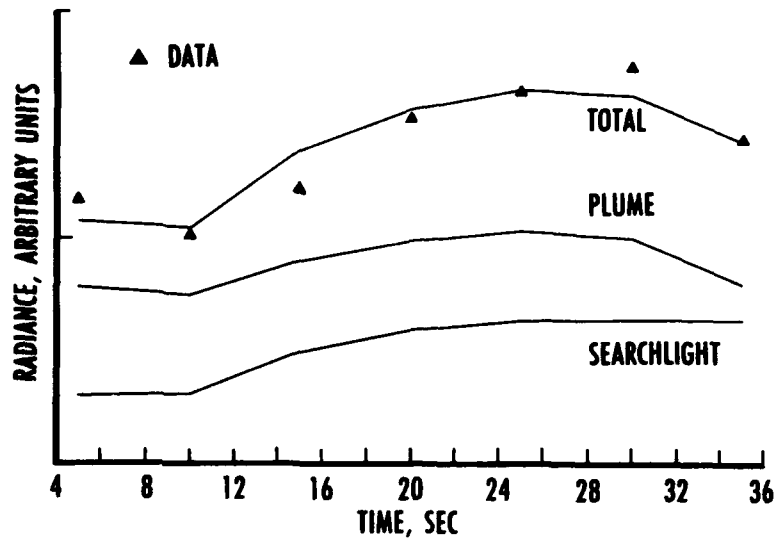


Figure 17. Decomposition of motor B radiance into searchlight and plume emission based upon calculated nozzle lip temperature time history.

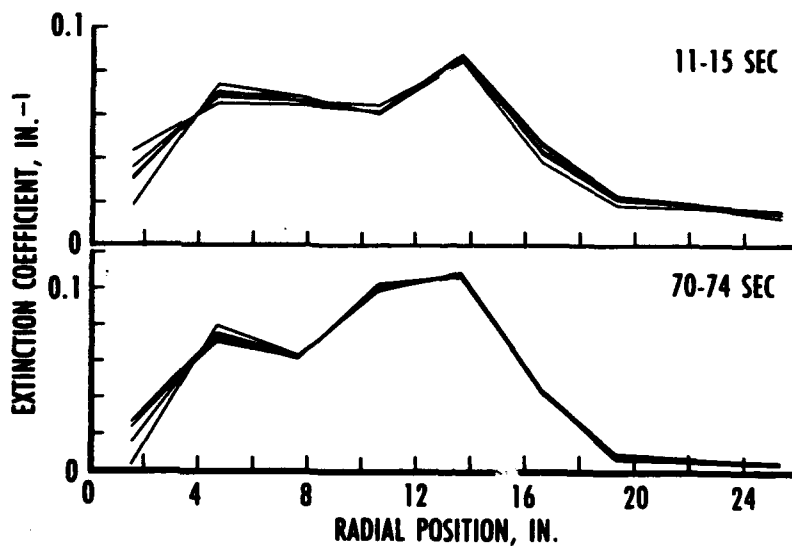


Figure 18. Extinction coefficient for motor A where inversions at approximately 1 sec intervals are shown near the beginning and the end of the burn.

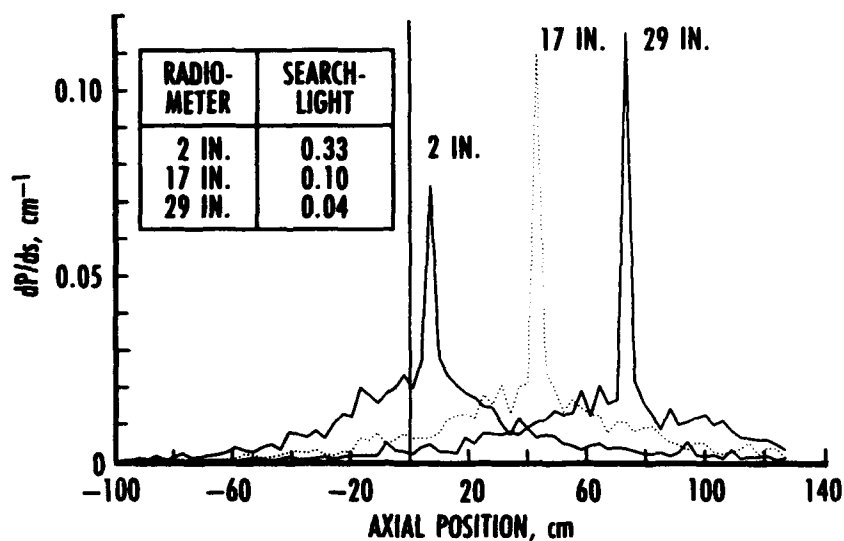


Figure 19. Monte Carlo calculation of searchlight for motor A for radiometers located at 2-, 17-, and 29-in. axial position where the nozzle exit plane is at 0 cm and the table gives searchlight view factor for each radiometer.

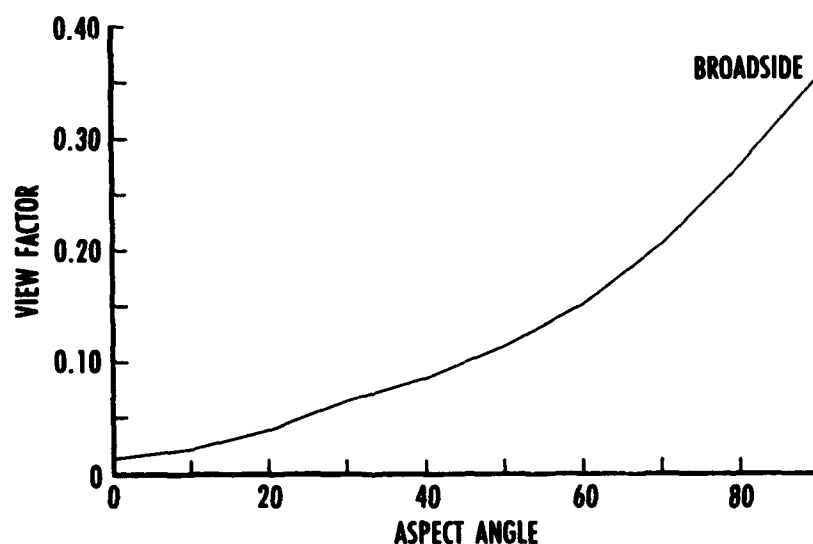


Figure 20. Monte Carlo calculation of searchlight view factor versus viewing aspect angle where radiometer location is 2 in. downstream of nozzle exit plane.

Table 1. Bandheads of the AlCl A<sup>1</sup>Π - X<sup>1</sup>Σ System

$\lambda$	$\bar{1}$	V,V	$\lambda$	$\bar{1}$	V,V
2708.9 R	2	R 7,9	2625.0 R	5	Q 3,3
2702.3 R	3	R 6,8	2622.4 R	4	R 3,3
2696.4 R	3	R 5,7	2620.0 R	4	Q 2,2
2692.8 R	5	Q 4,6	2618.2 R	3	R 2,2
2685.7 V	6	Q 2,4	2617.0 R	4	Q 1,1
2683.1 V	6	Q 1,3	2614.4 R	8	Q 0,0
2681.1 V	4	Q 0,2	2610.2 R	6	R 0,0
2649.7 V	4	Q 1,2	2606.7 R	2	R 6,5
2647.5 V	6	Q 0,1	2600.7 R	3	R 5,4
2644.9 R	2	R 7,7	2695.4 R	2	R 4,3
2638.1 R	3	R 6,6	2590.8 R	2	R 3,2
2632.8 R	3	Q 5,5	2586.7 R	2	R 2,1
2632.2 R	3	R 5,5	2564.3 R	1	R 4,2
2627.8 R	4	Q 4,4	2559.6 R	1	R 3,1
2627.0 R	3	R 4,4	2555.5 R	1	R 2,0

R 1,1

NOTE: THE LETTERS R AND V AFTER THE WAVELENGTH INDICATE THE DIRECTION OF DEGRADATION OF THE BAND, WHEREAS THE NATURE OF THE HEAD (R AND Q) IS INDICATED BEFORE THE VIBRATIONAL QUANTUM NUMBERS.

REF.: *THE IDENTIFICATION OF MOLECULAR SPECTRA*, R. W. B. PEARSE AND A. G. GAYDEN, CHAPMAN AND HALL LTD., 1950, p. 47.

**Table 2. Molecular Constants for the Ground and Resonant States of  $\text{Al}^{35}\text{Cl}$  ( $\text{cm}^{-1}$ )**

	$\text{X}^1\Sigma^+$	$\text{A}^1\Pi$
$T_e$	0	38254.0
$\omega_e^*$	481.30	449.96
$\omega_e x_e^*$	1.95	4.37
$\omega_e y_e^*$	---	-0.216
$B_e$	0.24393	0.259
$\alpha_e$	0.001611†	0.006
$D_e$	$2.503 \times 10^{-7}$	---
$\beta_e$	$-0.0053 \times 10^{-7}$	---

\* BASED UPON Q-BRANCH BANDHEADS

$$\dagger +4.697 \times 10^{-6}(v + \frac{1}{2})^2 - 4.7 \times 10^{-9}(v + \frac{1}{2})^3$$

**Table 3. Einstein Coefficients for the  $\text{A}^1\Pi - \text{X}^1\Sigma^+$  Transition in  $\text{AlCl}$  (Ref. 7).**

$v' \backslash v''$	0	1	2	3	4	5	6	7	8
0	1933	---	---	---	---	---	---	---	---
1	---	1890	---	---	---	---	---	---	---
2	---	7.92	18.32	---	---	---	---	---	---
3	---	---	3.3	1745	12	16.6	---	---	---
4	---	---	---	92	1578	37	31	---	---
5	---	---	---	---	200	1344	77	54	---
6	---	---	---	---	---	366	1028	121	87
7	---	---	---	---	---	---	574	658	149
8	---	---	---	---	---	---	18	766	301

ALL VALUES SHOULD BE MULTIPLIED BY  $10^5 \text{ sec}^{-1}$  (REF. 6)

VALUES NOT GIVEN ARE LESS THAN 0.5 PERCENT OF VALUE AT (0,0)



**Table 4. Constants for Dunham Level Expression of Energy Level of the X<sup>1</sup>Σ State of AlCl**

Molecular Constants for AlCl(X <sup>1</sup> Σ) used in Term Energy Expression: $T_{v,J} = \sum_{l,m} Y_{lm} (v + \frac{1}{2})^l J(J + 1)^m$			
		Y <sub>lm</sub>	
l	m	Al <sup>35</sup> Cl	Al <sup>37</sup> Cl
0	0	0.000000000000E+00	0.000000000000E+00
0	1	2.439300631168E-01	2.381908103047E-01
0	2	-2.501623484131E-07	-2.384688355076E-07
0	3	-4.247846717816E-14	-5.631834454137E-14
0	4	9.082196640775E-19	8.257101917000E-19
1	0	4.817765661053E+02	4.760760032685E+02
1	1	-1.611082122620E-03	-1.554551027648E-03
1	2	4.398230380075E-10	4.161398270080E-10
1	3	0.000000000000E+00	0.000000000000E+00
2	0	-2.101817969356E+00	-2.052568958832E+00
2	1	4.692056013898E-06	4.472534718003E-06
2	2	7.160332258952E-12	8.149446348886E-12
3	0	6.638164756386E-03	6.420867608319E-03
3	1	-5.291195847775E-05	-4.985420578000E-05
4	0	-2.023833735279E-05	-1.929715135000E-05

VALUES ARE IN UNITS OF CM<sup>-1</sup>